## PAPER

Check for updates

# Synergy of Ag and Pd in bimetallic catalysts for the selective oxidation of 5-(hydroxymethyl) furfural†

Dominik Neukum,[ab] Maya Eyleen Ludwig,[a] Georgios Uzunidis,[a] Ajai Raj Lakshmi Nilayam,[cd] Bärbel Krause, [e] Silke Behrens, [a] Jan-Dierk Grunwaldt [*ab] and Erisa Saraçi [*ab]

The synthesis of renewable bio-based monomers, like 2,5-furandicarboxylic acid (FDCA), is of high interest in the shift toward a circular economy. Bimetallic catalysts offer the variation of different properties, enabling the design of tailor-made catalysts. The combination of silver and palladium, both highly active for specific liquid-phase oxidation reactions, shows promise for superior performance in the selective oxidation of 5-(hydroxymethyl)furfural (HMF) to FDCA. While Ag/CBA and $Ag_3Pd_1$/CBA, supported on carbon black acetylene (CBA), were active only for the oxidation of the aldehyde group of HMF, increasing the Pd-fraction allowed for the oxidation of the alcohol group as well. In-depth characterization by X-ray diffraction, electron microscopy, and X-ray absorption spectroscopy revealed a synergistic effect between Ag and Pd in Pd-rich alloys, leading to an enhanced performance. Pd is particularly effective in activating oxygen, the oxidizing agent, while Ag ensures a high selectivity in the dehydrogenation reaction. Moreover, removing residual surfactants from the synthesized catalysts by increasing the calcination temperature further enhanced the activity. This study demonstrates the potential of tuning the catalytic properties of noble metal-based catalysts for optimizing liquid-phase oxidation reactions.

*a Institute of Catalysis Research and Technology, Karlsruhe Institute of Technology, Hermann-von-Helmholtz-Platz 1, 76344 Eggenstein-Leopoldshafen, Germany. E-mail: grunwaldt@kit.edu, erisa.saraci@kit.edu*

*b Institute for Chemical Technology and Polymer Chemistry, Karlsruhe Institute of Technology, Engesserstraße 20, 76131 Karlsruhe, Germany*

*c Institute of Nanotechnology, Karlsruhe Institute of Technology, Hermann-von-Helmholtz-Platz 1, 76344 Eggenstein-Leopoldshafen, Germany*

*d Karlsruhe Nano Micro Facility (KNMFi), Karlsruhe Institute of Technology, Hermann-von-Helmholtz-Platz 1, 76344 Eggenstein-Leopoldshafen, Germany*

*e Institute for Photon Science and Synchrotron Radiation, Karlsruhe Institute of Technology, Hermann-von-Helmholtz-Platz 1, 76344 Eggenstein-Leopoldshafen, Germany*

† Electronic supplementary information (ESI) available. See DOI: https://doi.org/10.1039/d4cy01028k
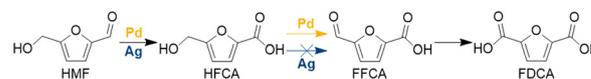
## Introduction

The growing demand for renewable chemicals to replace fossil-based materials has received significant attention in recent years. Lignocellulosic biomass, abundantly available from agricultural waste, serves as a valuable resource for producing various new platform molecules.[1,2] One particularly interesting example is 5-(hydroxymethyl)furfural (HMF), which can be selectively oxidized to 2,5-furandicarboxylic acid (FDCA), a potential replacement for terephthalic acid in the production of bio-based polyesters.[3–5] This promising monomer has not only attracted academic but also industrial attention, with various processes under development and Avantium's first flagship plant for production in industrial scale being close to operation.[6–8]

Multiple concepts have been explored for the oxidation of HMF, including homogeneously and heterogeneously catalysed processes.[6] Heterogeneous processes offer advantages, such as easier catalyst separation, and often utilize noble metal-based catalysts (Au, Pt, Pd, Ru), which enable the use of oxygen or air as a benign oxidant.[6,9,10] In an alkaline medium, the reaction typically proceeds *via* intermediates such as 5-(hydroxymethyl) furan-2-carboxylic acid (HFCA) and 5-formyl-2-furancarboxylic acid (FFCA; Scheme 1).[11]

The synthesis of bimetallic nanoparticles as active components can be applied to fine tune the electronic properties of noble metals, enabling improved properties, including catalytic activity or stability.[12–14] Recently, various bimetallic catalysts have been reported for the selective oxidation of HMF, including systems based on AuPd,[13,15–20] AuAg,[21,22] AuCu (ref. 23 and 24) or PtPd.[25] For example,



**Scheme 1** Reaction scheme for the selective oxidation of HMF to FDCA.

This journal is © The Royal Society of Chemistry 2024

*Catal. Sci. Technol.*, 2024, **14**, 7163–7171 | 7163

substituting a few Au atoms in an $Au_{25}$ cluster with Ag atoms (Au : Ag = 18.2 : 1) induced an electron transfer from Ag to Au, resulting in an enhanced activity for the dissociation of oxygen molecules in comparison to monometallic Au.[21] Similarly, Schade et al.[22] found an increased activity and stability against sintering for alloyed $Ag_3Au_7$ particles in HMF oxidation, with XPS and XAS characterization revealing enrichment of Ag at the surface of the particles. His finding is highly interesting as monometallic Ag-based catalysts have been reported to be inactive for the oxidation of the alcohol function in HMF, likely due to their inability to activate and dissociate oxygen molecules on the surface.[26,27]

To overcome this limitation, Beier et al.[28] utilized a physical mixture of $Ag/SiO_2$ and $CeO_2$ nanoparticles for the selective oxidation of benzyl alcohol to benzaldehyde, where metallic Ag-species were identified as the active species for alcohol dehydrogenation, while nanoparticulate $CeO_2$ took the role of activating molecular oxygen. However, $Ag/CeO_2$ catalysts were not active for the aqueous phase oxidation of HMF.[29] Huang et al.[30] showed that separated Au and Pd phases exhibit synergistic effects, with Pd responsible for activating molecular oxygen.

More recently, the application of bimetallic AgPd-based catalysts for different catalytic reactions has been proposed.[31–34] Jin et al.[31] reported the use of AgPd alloys supported on $CeO_2$ nanofibers, which resulted in a high FDCA yield of 93% with a 1 : 1 ratio of Ag and Pd under mild conditions (20 °C, 1 bar $O_2$ and a (Ag + Pd) : HMF ratio of 1 : 27). However, the FDCA yield declined drastically to <20% when switching the support material to other oxides, like $Al_2O_3$, $ZrO_2$ or $TiO_2$. These results suggest a strong influence of the nanoparticulate $CeO_2$ for the activation of oxygen at the catalyst surface. DFT calculations suggested that AgPd boundary sites had the lowest adsorption strength and the best catalytic activity compared to isolated Ag and Pd sites.

In this work, we present the selective oxidation of HMF using bimetallic AgPd nanoparticles supported on carbon black. The use of carbon black as a support material, with its low crystallinity and X-ray transparency, allowed for detailed characterization of the catalysts with different Ag-to-Pd ratios by techniques such as scanning transmission electron microscopy (STEM) coupled with energy dispersive X-ray spectroscopy (EDX), X-ray absorption spectroscopy (XAS), X-ray diffraction (XRD), and inductively coupled plasma-optical emission spectrometry (ICP-OES). These complementary techniques allowed us to determine structure–performance relationships for the bimetallic AgPd system in the oxidation of HMF. A synergistic behaviour of Ag and Pd in the particles was found, leading to enhanced catalytic activity for the bimetallic catalysts.

# Experimental

## Catalyst preparation

Unsupported Ag and Pd nanoparticles (NPs) as well as the bimetallic AgPd counterparts with different Ag : Pd ratios (3 : 1,

1 : 1, 1 : 3) were prepared according to a procedure based on protocols by Sun et al.[33] and Zhang et al.[35] Silver acetate (Ag(ac); $AgCH_3COO$) and palladium acetate (Pd(ac)$_2$; Pd(CH$_3$-COO)$_2$) at the specified ratio were dissolved in 10 mL of oleylamine (OLAM) at 70 °C until complete dissolution. The solution was heated to 180 °C under stirring. The temperature was kept for 1 h before being cooled to room temperature over about 1–2 h. The mechanism of nanoparticle formation including the reduction ability of oleylamine has been reported in the literature.[36,37] The freshly prepared nanoparticles were separated by centrifugation at 7830 rpm for 10 min and washed once with ethanol and twice with isopropanol. The particles were then redispersed in approximately 40 mL of cyclohexane. Carbon black acetylene (>99%, denoted as CBA) was added to the suspension, which was stirred for 1–2 h to facilitate supporting the particles. The resulting catalyst was separated from cyclohexane, dried in an oven overnight at 60 °C, and calcined at 200 °C (heating rate: 5 K min$^{-1}$) for 5 h in static air.

Moreover, a catalyst with an intended Ag : Pd ratio of 1 : 1 was prepared according to a modified approach of a method published by our group for comparison.[13] $AgNO_3$ (0.0159 g) and $Pd(NO_3)_2$ (0.0211 g) were dissolved in 350 mL $H_2O$. PVA ($m$(Ag + Pd) : $m$(PVA) = 1 : 1) was dissolved in 5 mL $H_2O$ and added to the solution. $NaBH_4$ ($n$($NaBH_4$) : $n$(Ag + Pd) = 4 : 1) was dissolved in about 5 mL $H_2O$ and added to the solution after about 10 min of stirring the solution. The formed suspension of colloidal nanoparticles was continuously stirred for about 30 min before adding carbon black Vulcan® XC72 (0.98 g) and adjusting the pH to 1 with 50 vol.% $H_2SO_4$. The nanoparticles immediately precipitated onto the support. Afterwards, the catalyst was filtered from the suspension and washed thoroughly with water.

## Catalyst characterization

Additional experimental information on the characterization methods can be found in the ESI.† For the analysis of the metal content, the catalysts were dissolved in 15 mL concentrated HCl using a microwave irradiation of 600 W for 90 min (Anton Paar Multiwave 3000). The digested samples were diluted with concentrated HCl, before being analysed by inductively coupled plasma-optical emission spectrometry (ICP-OES, Agilent 725 spectrometer, Agilent Technologies Inc.) with a plasma excitation of 40 MHz and 2 kW.

To determine the crystal structure of the noble metal-based nanoparticles, powder X-ray diffraction (XRD) was performed with a PANalytical X'pert Pro diffractometer using Cu-K$_\alpha$ radiation and a Ni filter. The scans were recorded in a $2\theta$-range from 5–120° or 5–80°. The data were processed with X'Pert HighScore by subtracting Cu-K$_{\alpha 2}$ radiation and the background. For the estimation of the crystallite size of the selected samples, the data were fitted with Origin2019 and the Scherrer equation (cf. ESI†) was applied.[38] LaB$_6$ was used as a reference.

Scanning transmission electron microscopy (STEM) was performed with a ThermoFisher Themis 300 (S)TEM, using a

high-angle annular dark-field (HAADF) detector for the collection of images of the supported nanoparticles. Energy Dispersive X-Ray (EDX) maps for estimating elemental distribution were acquired using a Super-X EDX detector. The powder catalysts were prepared on a standard Lacey carbon grid with a Cu mesh. Particle size distribution was determined with ImageJ software. Agglomerated particles were not taken into account for the particle size distribution analysis.

To estimate the degree of alloying and determine the oxidation state, X-ray absorption spectroscopy (XAS) was conducted on all catalysts at the CAT-ACT beamline at KIT Lightsource (Karlsruhe).[39] The spectra were recorded at Pd K-edge (24.35 keV) and Ag K-edge (25.514 keV) in transmission mode with ionization chambers with a beam size of 1 mm × 1 mm. A pair of Pt-coated Si mirrors rejected higher harmonics and a double-crystal monochromator with Si(311) crystal pairs was used for energy selection. For the measurements, the catalysts were densely packed as powder in a 6 mm diameter plastic tube. The recorded spectra were compared to those of Ag foil, Pd foil, and PdO references. Data processing and analysis was conducted using Athena from the Demeter software package (version 0.9.26).[40]

### HMF oxidation procedure

In a typical experiment, 10 mL of a 0.1 M HMF solution were added to a poly(tetrafluoroethylene) (PTFE) inset (50 mL volume) in an autoclave reactor. Prior to the reaction, a sample was taken for high-performance liquid chromatography (HPLC) analysis to determine the initial HMF concentration. Next, 212 mg of $Na_2CO_3$ (2 equivalents) and the catalyst (metal (M):HMF = 1:100) were added to the reactor. The autoclave was closed with a torque wrench, purged three times with synthetic air, and then pressurized at the specified reaction pressure (10–50 bar). The autoclave was subsequently heated to the respective reaction temperature (80–140 °C). Once the reaction temperature was reached, the reaction was allowed to proceed for 5 h. Afterwards, the autoclave was rapidly cooled down in an ice bath, depressurized, and opened. To calculate conversion, yields, and carbon-balance (C-balance), another sample (diluted 1:50) was taken for HPLC analysis. The C-balance included HMF and its oxidation products: HFCA, FFCA, and FDCA. HPLC was used to quantify the concentration of HMF, HFCA, FFCA, and FDCA. For the analysis, an Aminex HPX-87H column (BioRad Laboratories Inc.), a UV-vis detector, and 4 mM $H_2SO_4$ as an eluent were employed at 25 °C and a flow rate of 0.65 mL $min^{-1}$. Additional information on the materials and characterization methods can be found in the ESI.†

## Results and discussion

### Catalyst characterization

Catalysts with Ag:Pd ratios of 1:0, 3:1, 1:1, 1:3, and 0:1 were prepared and the metal loading of Ag and Pd was determined by ICP-OES (Table 1). The compositions of the different bimetallic samples were close to the intended ratios, and covered a broad range of Ag:Pd ratios. All catalysts

showed a slightly higher Ag-fraction than intended in the synthesis, with a deviation of about 10% for all bimetallic samples. This might be attributed to either an incomplete reduction of the Pd-precursor or a higher loss of Pd-rich particles during the centrifugation procedure.

TEM imaging was used to determine the mean particle diameter of the nanoparticles of the bimetallic AgPd-based catalysts. Previous studies on Au-based catalysts for the HMF oxidation have demonstrated that particle size can have a considerable influence on the catalytic activity.[41,42] In this study, an increase of the mean particle diameter with a higher Ag-fraction was observed (Fig. 1). Among the bimetallic samples, $Ag_1Pd_3$/CBA possessed the smallest mean particle diameter measuring 4.9 ± 1.5 nm. Particularly, both $Ag_1Pd_1$/CBA and $Ag_3Pd_1$/CBA displayed a bimodal particle size distribution, one fraction being very small (mean particle diameter of about 4.0 ($Ag_1Pd_3$) to 4.3 nm ($Ag_3Pd_1$)), while the other had a larger mean particle diameter (around 7.9 for $Ag_1Pd_1$ and 11.0 nm for $Ag_3Pd_1$). This bimodal distribution can also be seen in the histogram of the mean particle size of these two catalysts (cf. Fig. 1), where $Ag_1Pd_1$/CBA exhibited two distinct maxima. Additionally, a small share of larger particles was observed for $Ag_1Pd_3$/CBA. Despite these variations, nanoparticles with a diameter of about 4 nm were the most prevalent in the histogram for all catalysts. The bimodal particle size distribution might be caused by an earlier reduction of the Ag-precursor and a higher mobility of Ag atoms.

For Pd/CBA and Ag/CBA, the imaging showed predominantly agglomerated particles, limiting the evaluation to about 50 particles for each of these two catalysts (Fig. S1–S5†). Nonetheless, the particle size distributions of these two catalysts were consistent with the trends observed in the other catalysts. Pd/CBA exhibited the smallest nanoparticles with a mean diameter of 4.6 ± 0.9 nm and the narrowest particle size distribution with one distinct maximum. However, this came at the expense of significant agglomeration of Pd nanoparticles on the CBA support (Fig. S1 and S2†). In contrast, Ag/CBA had the largest mean particle diameter at 8.0 ± 4.0 nm with the broadest particle size distribution. These findings indicate that the addition of Ag leads to the formation of larger nanoparticles, a trend that will be further elucidated with the following characterization techniques.

To further study the chemical composition of the different particles, EDX-mapping was conducted on the selected regions

**Table 1** Ag and Pd loading of the catalysts as determined by ICP-OES

| Catalyst | Ag loading/wt% | Pd loading/wt% | Molar Ag-fraction in NPs/% | Intended Ag-fraction in NPs/% |
|---|---|---|---|---|
| Pd/CBA | 0 | 1.5 (±0.1) | 0 | 0 |
| $Ag_1Pd_3$/CBA | 0.6 (±0.1) | 1.1 (±0.1) | 35 | 25 |
| $Ag_1Pd_1$/CBA | 0.7 (±0.1) | 0.5 (±0.1) | 58 | 50 |
| $Ag_3Pd_1$/CBA | 1.9 (±0.8) | 0.3 (±0.1) | 87 | 75 |
| Ag/CBA | 2.9 (±0.1) | 0 | 100 | 100 |
| AgPd/C(BH) | 0.6 (±0.1) | 0.4 (±0.1) | 61 | 50 |
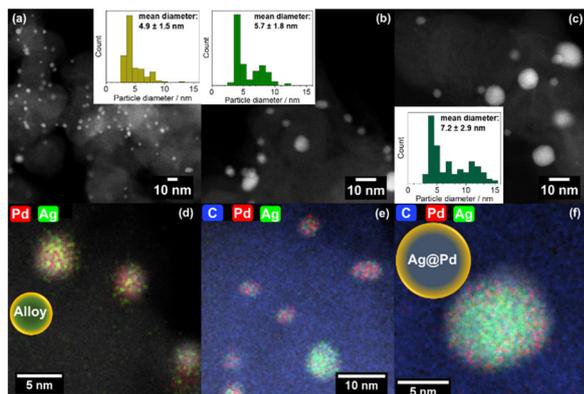
**Fig. 1** STEM images of (a) $Ag_1Pd_3$/CBA (particle count: 150), (b) $Ag_1Pd_1$/CBA (particle count: 139), and (c) $Ag_3Pd_1$/CBA (particle count: 153). EDX mapping of (d) $Ag_1Pd_3$/CBA, (e) $Ag_1Pd_1$/CBA, and (f) $Ag_3Pd_1$/CBA. The structure models were inserted as illustrations in (d) and (f). The particle size distribution is displayed as an inset in (a)–(c).

of the three bimetallic catalysts (Fig. 1). The images of $Ag_1Pd_1$/CBA and $Ag_3Pd_1$/CBA revealed an almost core–shell like structure of Ag@Pd for the bigger particles with a diameter of 7.9 to 11.0 nm (Fig. 1(c)), consisting of an Ag-rich core and a Pd-rich shell. This structure was further supported by line profile measurements (Fig. S6 and S7†). In contrast, smaller particles (4.0 to 4.3 nm) of all three catalysts displayed a higher Pd content compared to the intended ratio, but they were uniformly alloyed, with no evidence of a core–shell like structure. The $Ag_1Pd_3$/CBA catalyst was dominated by these smaller, Pd-rich alloyed particles. These findings provide valuable insights into the nature of the particles, which may explain their catalytic activity. However, it's important to note that EDX-mapping only examines a limited sample fraction, so no unequivocal conclusions can be drawn.

XRD analysis was conducted on both monometallic and bimetallic catalysts (Fig. 2), enabling the detection of metallic phases in the formed nanoparticles and elucidating the composition of the alloyed phases. The two monometallic catalysts showed reflections at 40.3° (Pd/CBA) and 38.2° (Ag/CBA) fitting to metallic fcc phases and closely resembling the references (Pd-reference from ICSD collection code 64915
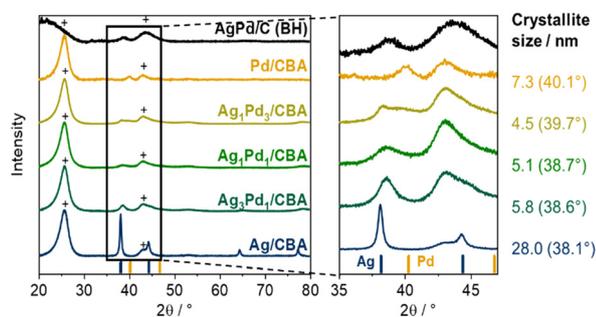
and Ag-reference from ICSD collection code 41690). The bimetallic catalysts gave broad reflections with a clearly visible shift in the reflection position. Apart from the metallic reflections, reflections of the C-based support materials were visible arising from graphite structures in the supports (26.6° and 44.6°). The introduction of Ag into the Pd lattice led to an expansion of the lattice parameters of the fcc phase, causing the (111) reflection to shift from 40.3° (Pd) to 38.2° (Ag, ICSD collection code 41690). However, overlapping reflections were obtained due to the presence of different particle types on the catalyst surface, as also observed with STEM-EDX. For $Ag_1Pd_3$/CBA, besides the main reflection of the smaller alloyed particles, an Ag-rich phase, likely resulting from Ag@Pd core–shell particles with an Ag-rich core, was visible. According to the fitting of the reflections, this is a minor fraction of the particles, which is in agreement with the results of the other characterization methods. A small fraction of bigger Ag-rich particles was expected due to the bimodal size distribution. The broad reflection of the smaller alloyed particles shifted towards the reflection of metallic Pd. In general, the reflections broadened with increasing Pd-fraction, implying the presence of smaller particles, which is in line with our findings by STEM. The crystallite size of the main noble metal peak, determined by the Scherrer equation, decreased accordingly from 5.8 nm ($Ag_3Pd_1$/CBA) to 4.5 nm ($Ag_1Pd_3$/CBA). The fitting of the reflections is shown in Fig. S8–S10.† In addition, a reference catalyst (AgPd/C (BH)) was prepared by reduction with $NaBH_4$. This reference catalyst showed a single distinct reflection for AgPd-particles at $2\theta$ = 38.9° ((111) reflection), which suggests the presence of only one kind of homogeneously alloyed particle. The position of the (111) reflection fits to a slightly more Ag-enriched phase than the intended 1:1 ratio, according to Vegard's law due to a deviation to a lower 2 theta angle.[43,44] The higher Ag-fraction was in agreement with ICP-OES, showing a molar fraction of Ag of 61% (Table 1).

To gain further information on the formation of the alloys and the oxidation state of Ag and Pd, XANES measurements were conducted on both monometallic and bimetallic catalysts at the Ag and Pd K-edges (Fig. 3). At both edges, the spectra of the catalysts resembled the features of the metallic
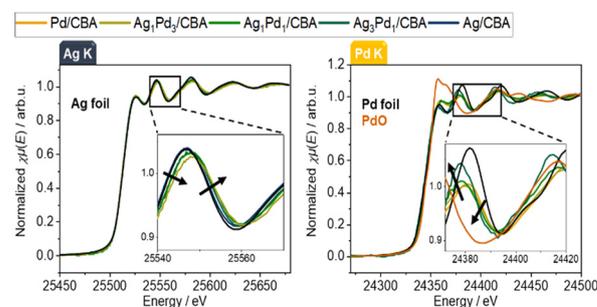


**Fig. 2** XRD patterns of the catalysts with magnification of the region of $2\theta$ = 35–47° (right). Graphite reference (+) is shown from ICSD collection code 230104. On the right side, the position of the (111) reflection and the estimation of the particle size from the FWHM are given.



**Fig. 3** XANES spectra of Pd/CBA, $Ag_1Pd_3$/CBA, $Ag_1Pd_1$/CBA, $Ag_3Pd_1$/CBA, and Ag/CBA measured at the Ag K-edge (left) and Pd K-edge (right). Metal foil and PdO references are shown.

**7166** | *Catal. Sci. Technol.*, 2024, **14**, 7163–7171

This journal is © The Royal Society of Chemistry 2024

foil references well, indicating that Ag and Pd are predominantly in a metallic state across all catalysts. At the Ag K-edge, a small shift of the features was observed with increasing Pd-fraction, suggesting the formation of alloyed phases. Similar observations have been reported in the literature for AgPd alloyed particles measured at the Ag K-edge and $L_3$-edge.[45,46] In general, the shift of the EXAFS features at the Pd K-edge to lower energies for a higher Ag content can be assigned to a change in the lattice parameters, specifically an expanded lattice due to incorporation of Ag in the crystal structure.[47] Interestingly, the shifts of the features were more pronounced at the Pd K-edge compared to the Ag K-edge, indicating that Pd was more significantly influenced in the bimetallic particles than Ag. This aligns with the observation that a higher Ag-fraction in the catalysts leads to the formation of large particles with a substantial Ag core and a thin Pd shell. The lattice parameters of the atoms in the Ag core remain relatively unaffected, resulting in only small shifts of the features at the Ag K-edge. In contrast, Pd atoms in the small alloyed nanoparticles and in the defect-rich, thin shell of the big particles are more affected by changes in the lattice parameters, leading to more pronounced shifts of the features in the XANES spectra. The data will be further analysed by EXAFS data analysis with alloyed, core–shell and monometallic particles.

## Influence of the Ag : Pd ratio on catalytic activity for the HMF oxidation

The catalysts with varying Ag : Pd ratios were tested for the HMF oxidation under the following conditions: 100 °C, 5 h, 10 bar air, 2 eq. $Na_2CO_3$, and M : HMF = 1 : 100. The results (Fig. 4) show that Ag/CBA only catalysed the aldehyde oxidation and did not produce any FDCA. This is in agreement with earlier studies for monometallic Ag-based catalysts.[29] On the other side, the Ag-rich bimetallic catalyst $Ag_3Pd_1$/CBA showed a considerable increase in the HFCA yield to 94.4%, underlining the substantial influence of Pd on Ag and the resulting change



**Fig. 4** HMF oxidation using Pd/CBA, $Ag_1Pd_3$/CBA, $Ag_1Pd_1$/CBA, $Ag_3Pd_1$/CBA, and Ag/CBA (100 °C, 5 h, 10 bar air, 2 eq. $Na_2CO_3$, M : HMF 1 : 100).

in the selectivity. Interestingly, the Ag@Pd core–shell like particles, which offer Pd atoms on the surface, were inactive for the alcohol oxidation, which is in contrast to the expected activity for monometallic Pd catalysts.[48–50] By further increasing the Pd-fraction in the catalyst, the main product switched from HFCA to FDCA. The highest FDCA yield of 66.9% was obtained with $Ag_1Pd_3$/CBA containing mostly alloyed nanoparticles. A further increase of the Pd-fraction led to a decrease of the FDCA yield to 33.8%. Thus, Ag atoms in the alloyed particles positively influence the selectivity compared to the monometallic Pd-based catalyst, also making the catalyst more cost-effective due to the significant price difference between Ag (0.92€ per g) and Pd (30.38€ per g; fabricated prices, effective 25.07.24).[51] Jin et al.[31] studied the ratio of Ag : Pd in bimetallic AgPd-based catalysts supported on nanoscale ceria. In contrast to our results, the highest FDCA yield was obtained with a 1 : 1 ratio of Ag and Pd. DFT calculations suggested lower adsorption energies of HMF on Ag–Pd boundaries.

Moreover, the C-balance of the catalysts was determined by taking HMF, HFCA, FFCA, and FDCA in the product solution into account. Hence, a high C-balance represents a low concentration of side products. These mainly occur by base-catalysed humin formation.[52] Interestingly, $Ag_1Pd_3$/CBA gave the highest C-balance of 100%, demonstrating its high activity for the oxidation reaction leading to the suppression of HMF degradation. In contrast, Ag/CBA had a C-balance of only 59%. This might be due to the larger particles giving an unfavourable surface-to-volume ratio, which results in an increase in side reactions. Similarly, Pd/CBA showed a decreased selectivity compared to $Ag_1Pd_3$/CBA, which is due to the lower selectivity of Pd compared to Ag.[28] The reduced selectivity might be due to side reactions like humin formation or decarbonylation.[52,53]

Ag-based catalysts have been reported to be highly selective for aldehyde oxidation in an alkaline medium.[26] Interestingly, Ag-based catalysts were found to be very selective in the benzyl alcohol oxidation in the presence of $CeO_2$ and $O_2$, suggesting that dissociated O-species play a crucial role in the alcohol oxidation mechanism over Ag.[28] This reaction also occurs via a dehydrogenation mechanism.[54] $CeO_2$ was proposed to provide O-species for the alcohol oxidation since Ag cannot dissociate $O_2$.[28] This role can also be taken by Pd.

In our case, a synergistic effect of Pd and Ag led to the improved selectivity compared to monometallic Pd (Fig. 5). Pd catalyses the dissociative adsorption of $O_2$.[30,55,56] Ag is highly selective in the dehydrogenation reactions; however, this reaction requires dissociated O-species to remove the hydrogen from the surface.[54] For this reason, Ag/CBA is not able to oxidise the alcohol function without sufficient Pd atoms present.[26,28] The O-species from Pd can free the surface of Ag from abstracted hydrogen atoms and regenerate the Ag-species. This improved selectivity of Ag explains that the monometallic Pd/CBA catalyst gave a lower C-balance compared to the bimetallic $Ag_1Pd_3$/CBA.
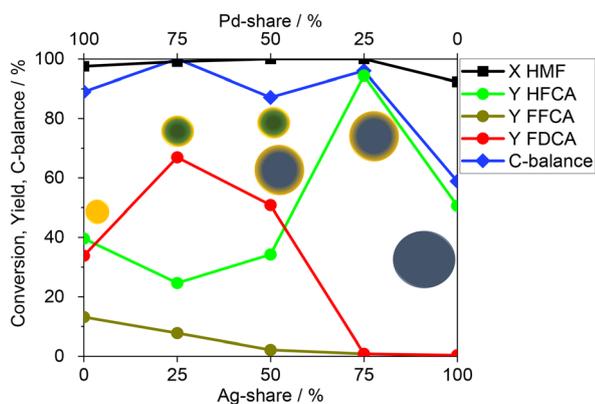
This journal is © The Royal Society of Chemistry 2024

*Catal. Sci. Technol.*, 2024, **14**, 7163–7171 | **7167**

## Alcohol oxidation



## Aldehyde oxidation

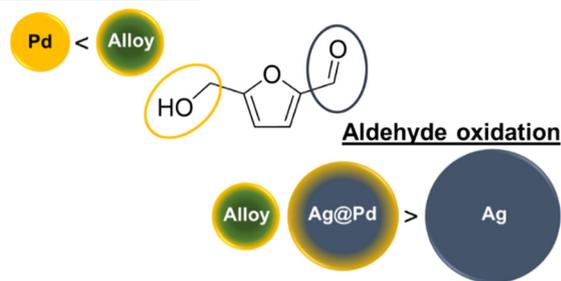**Fig. 5** Illustration of the proposed catalytic activity of Pd, Ag, AgPd alloy and Ag@Pd core–shell nanoparticles in HMF oxidation.



**Fig. 6** Investigation of the influence of (a) reaction temperature (5 h, 10 bar air, 2 eq. $Na_2CO_3$, M : HMF 1 : 100) and (b) reaction pressure (140 °C, 5 h, 2 eq. $Na_2CO_3$, M : HMF 1 : 200) over $Ag_1Pd_3$/CBA.

A synergistic effect of Pd and Ag in the small alloyed nanoparticles, including the dissociative adsorption of $O_2$ on Pd and the alcohol dehydrogenation on Ag, could have led to the enhanced selectivity compared to the monometallic catalysts. It has to be noted that variation in the particle size might influence the selectivity of the catalysts with an Ag-fraction of 50% or more. In addition, the change in the selectivity might be influenced by a redistribution of electron density at the interface of the two metals and within the alloy. Experimental and theoretical studies suggest that Pd gains electron density due to its higher electronegativity, while Ag loses net charge.[46,57] Nevertheless, both metals gain d-electrons, while losing electron density in the p- and s-orbitals.[46] These d-electrons are particularly important for the interaction with reactants, further enhancing the synergistic effect. In conclusion, Pd contributes significantly to the alcohol oxidation, as a hydrogen acceptor and by activation of molecular oxygen, which is an essential reactant in the dehydrogenation mechanism. Although Pd can catalyse both the alcohol and aldehyde oxidation, Ag has a way better selectivity for the oxidation steps resulting in decreased side reactions.

Moreover, it should be noted that geometric effects can influence the selectivity. Tang *et al.*[58] described surface and strain energy driven segregation of Ag and Pd in bimetallic AgPd nanoparticles. Ag-rich nanoparticles were shown to yield segregated isolated Pd-centers at the surface, while Pd-rich compositions lead to the formation of Pd ensembles consisting of multiple atoms. Such ensembles were reported to be required for the dissociation of oxygen.[59] Hence, only Pd-rich particles can activate oxygen. In contrast, isolated Pd-sites can form peroxide species.[59] These were hypothesized to be an important intermediate in the regeneration of hydroxide ions and the withdrawal of electrons from the metal surface.[60]

### Influence of temperature and air pressure during HMF oxidation

The influence of the reaction temperature and air pressure on the product composition was studied using $Ag_1Pd_3$/CBA by varying each parameter 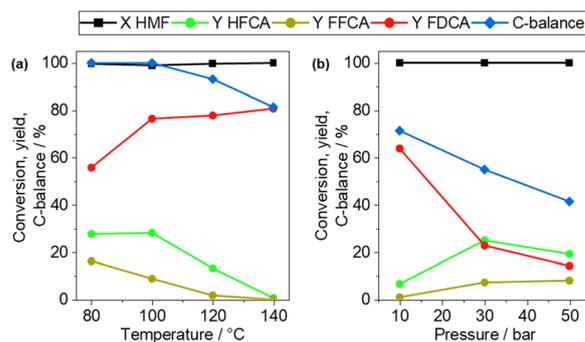separately (Fig. 6). Increasing the temperature resulted in a higher FDCA yield, reaching a maximum of 81.4% at 140 °C. At the same time, the C-balance decreased continuously, which can be attributed to an increased rate of side reactions leading to the degradation of HMF and the intermediates. This behaviour is in line with earlier studies on HMF oxidation.[11,29] For the investigation of the air pressure (Fig. 6(b)), the M : HMF ratio was switched to 1 : 200 as often increased FDCA yields and productivity were observed.[29,61] A FDCA yield of 63.9% was obtained at 140 °C and 10 bar. Reducing the catalyst mass led to a decrease of the FDCA yield from 80.8% to 63.9% (140 °C, 10 bar air), but increased the productivity from 16.2 $mol_{FDCA}$ $mol_{Ag+Pd}^{-1}$ $h^{-1}$ to 25.6 $mol_{FDCA}$ $mol_{Ag+Pd}^{-1}$ $h^{-1}$. This productivity surpasses that of several noble metal-based catalysts reported in the literature.[19,62,63]

Surprisingly, both the FDCA yield and C-balance decreased with increasing air pressure up to 50 bar, reaching a minimum FDCA-yield of 14.2%. This is in contrast with other studies on Ag- and Au-based catalysts, where a significant increase of the FDCA yield with increasing pressure was observed.[11,29,61] The reduction of the catalytic activity at higher air pressure might be attributed to the formation of PdO layers under these reaction conditions, causing the deactivation of the catalyst. Grunwaldt *et al.*[55] found that Pd particles re-oxidize on the surface in oxygen-saturated solvents during the oxidation of benzyl alcohol. The formed PdO showed a significantly lower reaction rate in the alcohol oxidation.[55] In contrast, an increase of the catalytic activity at enhanced pressure was reported for Ag-based catalysts in the oxidation of HMF, which were not influenced.[29] Hence, the alloyed particles undergo dynamic changes of the active species on the surface, resulting in the oxidation of Pd at high air pressure and the deactivation of the catalyst.[64] This result also points towards the important role of Pd in the dissociative adsorption of $O_2$.

XPS measurements of the fresh and spent $Ag_1Pd_3$/CBA catalyst (140 °C, 5 h, 50 bar air, 2 eq. $Na_2CO_3$, M : HMF 1 : 15) were performed. To improve the signal intensity of the XPS spectra, a catalyst with a loading of 10 wt% was prepared and separated after the reaction by centrifugation, followed by washing with ethanol and drying overnight. In line with the XANES analysis, the fresh catalyst showed

**7168** | *Catal. Sci. Technol.*, 2024, **14**, 7163–7171

This journal is © The Royal Society of Chemistry 2024

peaks of metallic Ag (368.2 eV, $3d_{5/2}$) and Pd (335.0 eV, $3d_{5/2}$) in the spectra (Fig. 7). The Pd peak showed a slight shift compared to the reference data (335.1 eV), which might be attributed to an interaction with the support material.[65] The spent catalyst showed no change of the Ag peak position. However, Pd showed an intense peak of PdO (337.5 eV) next to a peak of metallic Pd.[65] The intensity of the oxide peak can be attributed to a significant fraction of PdO at the surface. This proves the oxidation of Pd under high air pressure. Due to the inability of PdO to activate $O_2$ for the reaction, the catalyst deactivates in this state, leading to the lower FDCA-yield at increased pressure.

### Influence of the calcination temperature on the catalytic activity

To investigate the influence of organic residues on the catalyst's surface on the catalytic activity in HMF oxidation (100 °C, 5 h, 10 bar air, 2 eq. $Na_2CO_3$, M : HMF 1 : 100), $Ag_1$-$Pd_1$/CBA was calcined at 200 °C, 250 °C, and 300 °C. The FDCA yield increased by nearly 25% with rising calcination temperature (Fig. 8). Interestingly, no side products were observed for the catalysts calcined at 250 °C and 300 °C. The surfactants not only reduced the reaction rate for the HMF oxidation but probably also resulted in enhanced side reactions, causing HMF degradation and the formation of humins. Hence, residual surfactants on the catalyst surface hinder the oxidation of HMF. To account for the increase in noble metal loading after partial loss of the carbon-based support material during calcination in air, we determined the FDCA-productivity of the three catalysts, by normalizing to the metal loading. The normalized FDCA productivity increased from 10.1 to 12.2 $mol_{FDCA}$ $mol_{Ag+Pd}^{-1}$ $h^{-1}$ as the calcination temperature rose from 200 to 300 °C. Changes in particle size due to sintering at higher calcination temperature might influence the activity, which will be studied in the near future. Moreover, an oxidation reaction with the catalyst calcined at 200 °C and the addition of 4 eq.
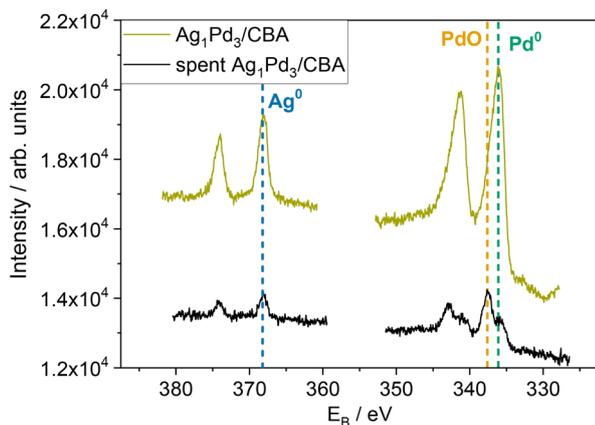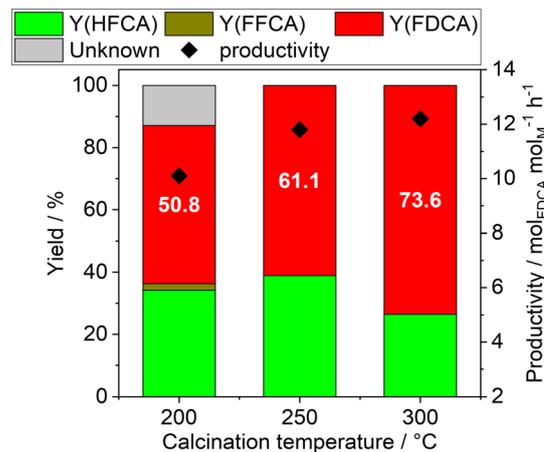


**Fig. 8** HMF oxidation (100 °C, 5 h, 10 bar air, 2 eq. $Na_2CO_3$, M : HMF 1 : 100) with $Ag_1Pd_1$/CBA calcined at 200, 250, and 300 °C. HFCA, FFCA, and FDCA yields are shown on the left y-axis and the FDCA-productivity (♦) is shown on the right y-axis.

oleylamine (100 °C, 5 h, 10 bar air, 2 eq. $Na_2CO_3$, M : HMF 1 : 100) was performed. The addition of oleylamine resulted in an almost complete deactivation of the catalyst with an HFCA yield of 3% and an FDCA yield of 0% at an HMF conversion of 85%, emphasising the negative influence of the surfactant on the catalytic performance. The presence of residual organic compounds on the surface of the catalyst was further addressed by thermogravimetric analysis (cf. ESI,† Fig. S11).

At 250 °C and 300 °C, mass losses of about 3 wt% and 30 wt% were observed, respectively. These losses probably occurred due to the degradation and desorption of the surfactant in addition to the partial decomposition of the support material. However, we assume that no noble metal was lost during this process. The calcination at higher temperatures was not feasible due to an almost complete degradation of the support material. When using carbon-based support materials, 300 °C was the optimal calcination temperature to increase the activity of the catalyst while avoiding complete decomposition of the support material. The influence is expected to be the same for all catalysts studied in this work.

## Conclusion

The variation of the Ag : Pd ratio for the catalytic oxidation of HMF to FDCA unravelled a strong synergistic effect of Ag and Pd leading to enhanced catalytic activity and selectivity of $Ag_1Pd_3$/CBA compared to Pd/CBA. This effect might be related to the dissociative adsorption of molecular oxygen involving Pd atoms, while Ag is highly active and selective in the dehydrogenation reaction. The dissociated O-species facilitate the removal of abstracted hydrogen atoms from the catalyst particles and the regeneration of Ag. $Ag_1Pd_3$/CBA was mainly composed of Pd-rich alloyed particles, which seem to be ideal for the oxidation of the alcohol and aldehyde functions of HMF. A shift of the selectivity of the main



**Fig. 7** Ag (left) and Pd (right) 1s XPS spectra of fresh and spent $Ag_1Pd_3$/CBA.

This journal is © The Royal Society of Chemistry 2024

Catal. Sci. Technol., 2024, **14**, 7163–7171 | **7169**

product from HFCA to FDCA occurred at an Ag-fraction below 75% due to the synergy of Ag and Pd. Catalyst deactivation at increased air pressure, presumably due to the formation of PdO at the surface, further indicates the important interaction of Pd with molecular oxygen.

At a high Ag-fraction, mostly Ag@Pd core–shell particles were formed. These particles showed high reaction rates for the aldehyde oxidation but failed to oxidize the alcohol function. The Pd-rich layer on the outer surface was deactivated for the alcohol oxidation, which might be related to an overoxidation of Pd leading to the formation of less active PdO. We further found that the calcination temperature played an important role. Higher calcination temperatures were beneficial and probably allowed a better accessibility of the noble metal particles due to the removal of residual surfactants. Future studies on the synthesis approach for bimetallic particles to achieve the sole formation of the catalytically most active Pd-rich alloy might lead to an enhanced catalytic activity.

## Data availability

Data are published at the KITOpen repository under the following link (**https://doi.org/10.35097/zgsgqvm54xhvjdg8**).

## Author contributions

The manuscript was written through contributions of all authors. All authors have given approval to the final version of the manuscript.

## Conflicts of interest

There are no conflicts to declare.

## Acknowledgements

## Notes and references

1 A. Corma, S. Iborra and A. Velty, *Chem. Rev.*, 2007, **107**, 2411–2502.

2 J. J. Bozell and G. R. Petersen, *Green Chem.*, 2010, **12**, 539–554.

3 A. F. Sousa, C. Vilela, A. C. Fonseca, M. Matos, C. S. R. Freire, G.-J. M. Gruter, J. F. J. Coelho and A. J. D. Silvestre, *Polym. Chem.*, 2015, **6**, 5961–5983.

4 E. de Jong, M. A. Dam, L. Sipos and G. J. Gruter, in *Biobased Monomers, Polymers, and Materials*, American Chemical Society, 2012, ch. 1, vol. 1105, pp. 1–13.

5 R.-J. van Putten, J. C. van der Waal, E. de Jong, C. B. Rasrendra, H. J. Heeres and J. G. de Vries, *Chem. Rev.*, 2013, **113**, 1499–1597.

6 M. Sajid, X. Zhao and D. Liu, *Green Chem.*, 2018, **20**, 5427–5453.

7 H. Liu, X. Tang, X. Zeng, Y. Sun, X. Ke, T. Li, J. Zhang and L. Lin, *Green Energy Environ.*, 2022, **7**, 900–932.

8 G. Totaro, L. Sisti, P. Marchese, M. Colonna, A. Romano, C. Gioia, M. Vannini and A. Celli, *ChemSusChem*, 2022, **15**, e202200501.

9 S. Hameed, L. Lin, A. Wang and W. Luo, *Catalysts*, 2020, **10**, 120.

10 Z. Zhang and K. Deng, *ACS Catal.*, 2015, **5**, 6529–6544.

11 O. Casanova, S. Iborra and A. Corma, *ChemSusChem*, 2009, **2**, 1138–1144.

12 F. Liu, D. Wechsler and P. Zhang, *Chem. Phys. Lett.*, 2008, **461**, 254–259.

13 D. Neukum, L. Baumgarten, D. Wüst, B. B. Sarma, E. Saraçi, A. Kruse and J.-D. Grunwaldt, *ChemSusChem*, 2022, **15**, e202200418.

14 H. Xin, A. Vojvodic, J. Voss, J. K. Nørskov and F. Abild-Pedersen, *Phys. Rev. B: Condens. Matter Mater. Phys.*, 2014, **89**, 115114.

15 Z. Gao, R. Xie, G. Fan, L. Yang and F. Li, *ACS Sustainable Chem. Eng.*, 2017, **5**, 5852–5861.

16 X. Wan, C. Zhou, J. Chen, W. Deng, Q. Zhang, Y. Yang and Y. Wang, *ACS Catal.*, 2014, **4**, 2175–2185.

17 A. Villa, M. Schiavoni, S. Campisi, G. M. Veith and L. Prati, *ChemSusChem*, 2013, **6**, 609–612.

18 A. Lolli, S. Albonetti, L. Utili, R. Amadori, F. Ospitali, C. Lucarelli and F. Cavani, *Appl. Catal., A*, 2015, **504**, 408–419.

19 Z. Gui, W. Cao, S. Saravanamurugan, A. Riisager, L. Chen and Z. Qi, *ChemCatChem*, 2016, **8**, 3636–3643.

20 D. Neukum, A. R. Lakshmi Nilayam, M. E. Ludwig, A. A. Vadarlis, J.-D. Grunwaldt and E. Saraçi, *Catal. Sci. Technol.*, 2024, **14**, 2130–2138.

21 Z. Liu, Y. Tan, J. Li, X. Li, Y. Xiao, J. Su, X. Chen, B. Qiao and Y. Ding, *Green Chem.*, 2022, **24**, 8840–8852.

22 O. R. Schade, F. Stein, S. Reichenberger, A. Gaur, E. Saraçi, S. Barcikowski and J.-D. Grunwaldt, *Adv. Synth. Catal.*, 2020, **362**, 5681–5696.

23 S. Albonetti, T. Pasini, A. Lolli, M. Blosi, M. Piccinini, N. Dimitratos, J. A. Lopez-Sanchez, D. J. Morgan, A. F. Carley, G. J. Hutchings and F. Cavani, *Catal. Today*, 2012, **195**, 120–126.

**7170** | *Catal. Sci. Technol.*, 2024, **14**, 7163–7171

This journal is © The Royal Society of Chemistry 2024

24  G. Uzunidis, O. Schade, D. Schild, J.-D. Grunwaldt and S. Behrens, *ChemNanoMat*, 2021, **7**, 1108–1116.

25  H. Choudhary and K. Ebitani, *Chem. Lett.*, 2016, **45**, 613–615.

26  O. R. Schade, A. Gaur, A. Zimina, E. Saraçi and J.-D. Grunwaldt, *Catal. Sci. Technol.*, 2020, **10**, 5036–5047.

27  J. An, G. Sun and H. Xia, *ACS Sustainable Chem. Eng.*, 2019, **7**, 6696–6706.

28  M. J. Beier, T. W. Hansen and J.-D. Grunwaldt, *J. Catal.*, 2009, **266**, 320–330.

29  O. R. Schade, K. F. Kalz, D. Neukum, W. Kleist and J.-D. Grunwaldt, *Green Chem.*, 2018, **20**, 3530–3541.

30  X. Huang, O. Akdim, M. Douthwaite, K. Wang, L. Zhao, R. J. Lewis, S. Pattisson, I. T. Daniel, P. J. Miedziak, G. Shaw, D. J. Morgan, S. M. Althahban, T. E. Davies, Q. He, F. Wang, J. Fu, D. Bethell, S. McIntosh, C. J. Kiely and G. J. Hutchings, *Nature*, 2022, **603**, 271–275.

31  Y. Jin, S. Sarina, H. Liu, W. Martens, E. R. Waclawik, E. Peiris, J. Jia, J. Shang, L. Kou, C. Guo and H.-Y. Zhu, *ACS Catal.*, 2022, **12**, 11226–11238.

32  G. Uzunidis and S. Behrens, *Chem. Ing. Tech.*, 2022, **94**, 328–339.

33  D. Sun, P. Li, B. Yang, Y. Xu, J. Huang and Q. Li, *RSC Adv.*, 2016, **6**, 105940–105947.

34  L. Li, Z. Niu, S. Cai, Y. Zhi, H. Li, H. Rong, L. Liu, L. Liu, W. He and Y. Li, *Chem. Commun.*, 2013, **49**, 6843–6845.

35  S. Zhang, Ö. Metin, D. Su and S. Sun, *Angew. Chem., Int. Ed.*, 2013, **52**, 3681–3684.

36  S. Mourdikoudis and L. M. Liz-Marzán, *Chem. Mater.*, 2013, **25**, 1465–1476.

37  M. Chen, Y.-G. Feng, X. Wang, T.-C. Li, J.-Y. Zhang and D.-J. Qian, *Langmuir*, 2007, **23**, 5296–5304.

38  P. Scherrer, *Nachr. Ges. Wiss. Goettingen, Math.-Phys. Kl.*, 1918, 98–100.

39  A. Zimina, K. Dardenne, M. A. Denecke, J. D. Grunwaldt, E. Huttel, H. Lichtenberg, S. Mangold, T. Pruessmann, J. Rothe, R. Steininger and T. Vitova, *J. Phys.: Conf. Ser.*, 2016, **712**, 012019.

40  B. Ravel and M. Newville, *J. Synchrotron Radiat.*, 2005, **12**, 537–541.

41  O. Schade, P. Dolcet, A. Nefedov, X. Huang, E. Saraçi, C. Wöll and J.-D. Grunwaldt, *Catalysts*, 2020, **10**, 342.

42  C. Megías-Sayago, A. Lolli, D. Bonincontro, A. Penkova, S. Albonetti, F. Cavani, J. A. Odriozola and S. Ivanova, *ChemCatChem*, 2020, **12**, 1177–1183.

43  L. Vegard, *Z. Med. Phys.*, 1921, **5**, 17–26.

44  C. Hahn, D. N. Abram, H. A. Hansen, T. Hatsukade, A. Jackson, N. C. Johnson, T. R. Hellstern, K. P. Kuhl, E. R. Cave, J. T. Feaster and T. F. Jaramillo, *J. Mater. Chem. A*, 2015, **3**, 20185–20194.

45  M. R. Ball, K. R. Rivera-Dones, E. B. Gilcher, S. F. Ausman, C. W. Hullfish, E. A. Lebrón and J. A. Dumesic, *ACS Catal.*, 2020, **10**, 8567–8581.

46  I. Coulthard and T. K. Sham, *Phys. Rev. Lett.*, 1996, **77**, 4824–4827.

47  J. A. Zamora Zeledón, M. B. Stevens, G. T. K. K. Gunasooriya, A. Gallo, A. T. Landers, M. E. Kreider, C. Hahn, J. K. Nørskov and T. F. Jaramillo, *Nat. Commun.*, 2021, **12**, 620.

48  B. Siyo, M. Schneider, J. Radnik, M.-M. Pohl, P. Langer and N. Steinfeldt, *Appl. Catal., A*, 2014, **478**, 107–116.

49  S. Saxena, D. Yadaw, K. Tiwari, V. Venkatesh, S. Verma, R. G. S. Pala and S. Sivakumar, *Catal. Lett.*, 2021, **151**, 921–931.

50  B. Siyo, M. Schneider, M.-M. Pohl, P. Langer and N. Steinfeldt, *Catal. Lett.*, 2014, **144**, 498–506.

51  Heraeus, Heraeus Precious Metal Prices - Current, **https://www.heraeus.com/de/hpm/market_reports/prices/historical_hu.html**, (accessed 25.07.2024, 2024).

52  I. van Zandvoort, Y. Wang, C. B. Rasrendra, E. R. H. van Eck, P. C. A. Bruijnincx, H. J. Heeres and B. M. Weckhuysen, *ChemSusChem*, 2013, **6**, 1745–1758.

53  Q. Meng, D. Cao, G. Zhao, C. Qiu, X. Liu, X. Wen, Y. Zhu and Y. Li, *Appl. Catal., B*, 2017, **212**, 15–22.

54  T. Mallat and A. Baiker, *Chem. Rev.*, 2004, **104**, 3037–3058.

55  J.-D. Grunwaldt, M. Caravati and A. Baiker, *J. Phys. Chem. B*, 2006, **110**, 25586–25589.

56  M. Besson and P. Gallezot, *Catal. Today*, 2000, **57**, 127–141.

57  Z. W. Lu, S. H. Wei and A. Zunger, *Phys. Rev. B: Condens. Matter Mater. Phys.*, 1991, **44**, 10470–10484.

58  J. Tang, L. Deng, H. Deng, S. Xiao, X. Zhang and W. Hu, *J. Phys. Chem. C*, 2014, **118**, 27850–27860.

59  L. Ouyang, G.-j. Da, P.-f. Tian, T.-y. Chen, G.-d. Liang, J. Xu and Y.-F. Han, *J. Catal.*, 2014, **311**, 129–136.

60  S. E. Davis, B. N. Zope and R. J. Davis, *Green Chem.*, 2012, **14**, 143–147.

61  D. Neukum, E. Saraçi, D. Wüst, A. R. Lakshmi Nilayam, S. Sharma and J.-D. Grunwaldt, *Catal. Today*, 2024, **432**, 114615.

62  J. Cai, H. Ma, J. Zhang, Q. Song, Z. Du, Y. Huang and J. Xu, *Chem. – Eur. J.*, 2013, **19**, 14215–14223.

63  C. A. Antonyraj, N. T. T. Huynh, S.-K. Park, S. Shin, Y. J. Kim, S. Kim, K.-Y. Lee and J. K. Cho, *Appl. Catal., A*, 2017, **547**, 230–236.

64  K. F. Kalz, R. Kraehnert, M. Dvoyashkin, R. Dittmeyer, R. Gläser, U. Krewer, K. Reuter and J.-D. Grunwaldt, *ChemCatChem*, 2017, **9**, 17–29.

65  J. F. Moulder and J. Chastain, *Handbook of X-ray Photoelectron Spectroscopy: A Reference Book of Standard Spectra for Identification and Interpretation of XPS Data*, Physical Electronics Division, Perkin-Elmer Corporation, Eden Prairie, Minnesota, 1992.

This journal is © The Royal Society of Chemistry 2024

*Catal. Sci. Technol.*, 2024, **14**, 7163–7171 | **7171**